Chapter 2

Optical Properties of Multiferroic $BiFeO_3$ Films

Hiromi Shima, Hiroshi Naganuma and
Soichiro Okamura

Additional information is available at the end of the chapter

http://dx.doi.org/10.5772/54908

1. Introduction

1.1. Background

Lightwave communication systems are predominantly used for handling high-speed data traffic. Long-distance ground-based systems particularly depend on optical fibers. Several business and research facilities employ direct fiber connections, and fiber to the home (FTTH) technology is foreseeable in the near future. These developments are driven particulary by the high demand for bandwidth necessary for many computers contributing to internet traffic. Lightwave communication systems are one of the fastest growing industrial fields because of a few important inventions and extensive research and development by physicists and engineers. The key components of a long-distance lightwave communication system are semiconductor lasers, low-loss glass fibers, optical amplifiers, and photodetectors. Apart from these key elements, several additional functions are required to enable modulating, switching, and combining the optical signals. In addition, network traffic management and switching, routing, and distribution systems are essential. Therefore, we focused on the development of optical components such as modulators and switches.

Here, some of the novel optical devices for modulating or switching light signals are introduced. First, the operating principle of an electro-optic spatial light modulator (EOSLM) is described. In general, a spatial light modulator is an optical device that achieves spatial modulation of incident light. Figure 1(a) shows the basic structure of an optical switching cell in an EOSLM. [1, 2] An electro-optic thin film is fabricated on a large-scale integration (LSI) circuit together with top and bottom electrodes. The top electrode is made of transparent conductive material such as indium tin oxide (ITO). A dielectric multi-layer mirror (DMM) is deposited onto the ITO electrode, and a Fabry-Perot resonator is formed between the upper mirror and the bottom platinum electrode. In this case, the minimum reflectance becomes zero

because the reflectance of the DMM and the bottom Pt layer is the same. If the refractive index can be controlled by applying an electric field, the cell can switch incident light at a specific wavelength as shown in Fig. 1(b).

Next, the operating principle of a Mach-Zehnder modulator (MZM) is described. Figure 2 shows a schematic diagram of an electrooptic-type MZM. [3-5] Incident light is split into two waveguides. The output amplitude depends on the phase difference at recombination. As shown in the top right part of the figure, in-phase recombination produced a "1" bit output while anti-phase recombination produces a "0" bit output owing to half-wave phase shifting caused by an applyied voltage. A half-wave phase shift can be caused by either the electro-optic effect or the thermo-optic effect. When using the thermo-optic effect, the optical switch structure includes a heater on one side of the waveguide instead of a top electrode. [6,7]

To realize these novel thin-film optical devices, many researchers have intensively studied materials that exhibit the electro-optic effect. Traditional electro-optic materials include (Pb,La)(Zr,Ti)O_3 (PLZT) and $LiNbO_3$. PLZT is the most promising candidate for such applications because it has a high transparency in its polycrystalline form. [7] It is well known that bulk PLZT with a 65:35 Zr:Ti ratio shows large electro-optic e ▪ ect coe ▪ cients: a Pockels coe ▪ cient (linear electro-optic coe ▪ cient) of 6.12×10^{-10} m/V and a Kerr coe ▪ cient (quadratic electro-optic coe ▪ cient) of 9.12×10^{-16} m^2/V^2 with La contents of 8 and 9 at.%, respectively. [8] The next generation of new multiferroic materials, such as $BiFeO_3$ (BFO), which exhibits a giant remanent polarization of 100 μC/cm^2 in the thin-film form, [9,10] is now reaching maturity and has recently attracted considerable attention because of its potential applications in novel multifunctional devices. In recent years, the electric and magnetic properties of BFO films have been a topic of intense research, with regard to their magnetoelectric (ME) effect [11-13], while few reports on their optical properties have been published. [14-16] Therefore, it is necessary to know the basic optical properties of BFO films, such as the optical constant and thermooptic property, for the development of various optical applications. Understanding the optical potential in multiferroic materials leads us to additional noble material selections and thus degrees of freedom.

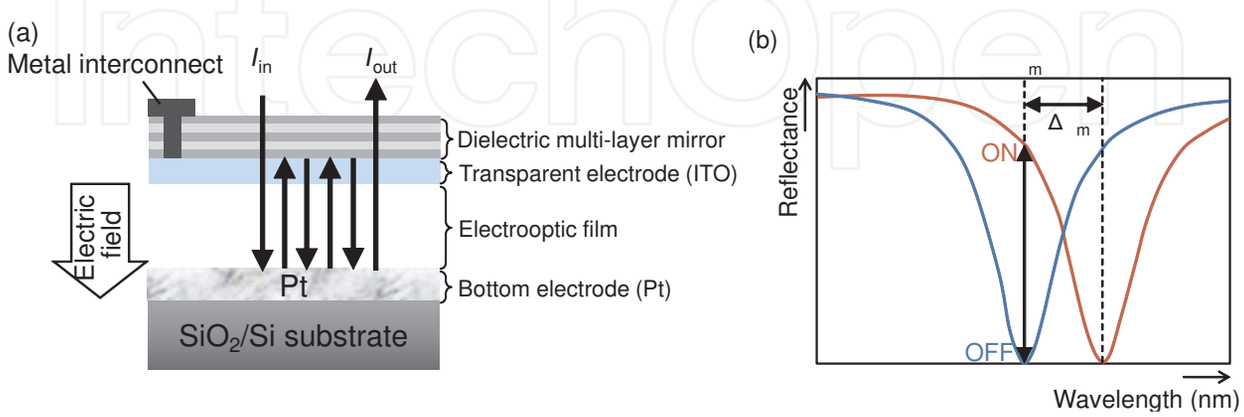

Figure 1. (a) Cross-sectional view of optical switching cell structure of the EOSLM, and 1(b) simulated optical switching properties of unit cells.

http://dx.doi.org/10.5772/54908

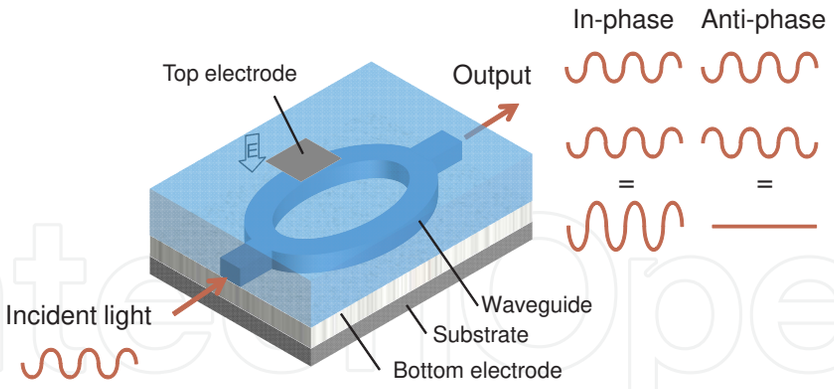

Figure 2. Schematic illustration of the electrooptic-type Mach-Zehnder modulator.

1.2. Objectives

To realize smaller and faster optical modulators or switches, it is necessary to embed electro-optic or thermo-optic materials in semiconductor integrated circuits. Accordingly, we have investigated the electro-optic and thermo-optic coefficients of materials in polycrystalline film form. We explain in detail the optical property evaluation method used in this study to exclude extrinsic effects, and then, we carefully determine the basic optical and thermo-optical properties of multiferroic $BiFeO_3$ polycrystalline films. Finally, we would like to understand the potential application of these optical properties to noble multifunctional devices using multiferroic $BiFeO_3$ polycrystalline films. This chapter describes the basic film preparation method and the basic method for evaluation of optical properties to increase understandings for beginner in this research field.

1.3. Outline of this chapter

This chapter is divided into 4 sections. Section 1 describes the background and objective of this study. In Section 2, we summarize the fundamentals of multiferroic $BiFeO_3$ used in this study, the method for fabricating multiferroic thin films, the basic optics principles related to this study, and the detailed method for evaluating optical properties. In Section 3, we discuss the thermooptic effect of multiferroic BFO films. The polycrystalline BFO films are fabricated on $Pt/Ti/SiO_2/Si$ substrates, respectively. First, their fundamental properties are evaluated. Next, the optical constants of these films are evaluated as a basic optical property. In Section 4, we summarize the conclusions of this chapter.

2. Experimental procedures

2.1. Fundamentals

Ferroelectricity is a property of certain materials that allows for spontaneous reversible electric polarization by applying an external electric field. The ability of a crystal to exhibit spontaneous

polarization is related to its symmetry. Of the 32 point groups, which describe all crystalline systems, 11 are centrosymmetric and contain an inversion center. The remaining 21 point groups without an inversion center can exhibit piezoelectricity, except for the point group *432*. Among the 21 groups without an inversion center, 10 polar groups possess a unique polar axis. Such asymmetric crystals can show unique electrical as well as optical characteristics, *e.g.*, the electro-optic effect, acousto-optic effect, photorefractive effect, nonlinear optical effect, etc. It is possible to control light dynamically using these effects to change the refractive index of materials.

In this chapter, the fundamentals of materials, fabrication, and evaluation are mentioned. In particular, the basic characteristics of $BiFeO_3$ potential ferroelectric films are mentioned together with their optical properties.

2.2. $BiFeO_3$ multiferroics

Perovskite-oxide has a structural formula of ABO_3, in which A is a large cation such as Bi^{3+}, Ba^{2+}, or Pb^{2+}, and B is a medium-sized cation such as Fe^{3+}, Ti^{4+}, or Zr^{4+}. These cations are located in cages formed by a network of oxygen anions, as shown in Fig. 3(a). Ferroelectric perovskites are a subgroup of the perovskite family. They are cubic at high temperatures and become polar non-cubic, *i.e.*, tetragonal, rhombohedral, *etc.*, below their Curie temperature. In the cubic phase, the cations are located at the center of an oxygen octahedron, while in the polar phases, they are shifted off center. The direction of the displacement of the cations in oxygen can be switched by applying an electric field, as shown in Fig. 3(b).

Multiferroic materials have more than one primary ferroic order parameter such as ferroelectricity, ferromagnetism, and ferroelasticity in the same phase. Multiferroic materials have attracted considerable attention, not only in terms of scientific interest but also because of their potential applications in novel functional devices. Bismuth ferrite ($BiFeO_3$, BFO) has long been known to be a multiferroic material that exhibits antiferromagnetism ($T_N \approx 643$ K) [17] and ferroelectricity ($T_C \approx 1103$ K) [18] when in bulk form. The structure and properties of thesingle-crystal form of BFO have been extensively studied. It has a rhombohedrally distorted perovskite structure with space group *R*3*c* [19] at room temperature (RT), as shown in Fig. 4. A perovskite-type unit cell with a rhombohedral structure has a lattice parameter of $a = b = c =$ 0.3965 nm and $\alpha = 89.3^{o}$ at RT. [19,20]

The Fe magnetic moments are coupled ferromagnetically within the pseudocubic (111) planes and antiferromagnetically between the near planes; this is called the *G*-type antiferromagnetic order. If the magnetic moments are oriented perpendicular to the [111] direction, the symmetry also permits a canting of the antiferromagnetic sublattices resulting in a macroscopic magnetization called weak magnetism. [21,22]

According to a first-principles calculation, the spontaneous polarization of BFO changes depending on whether the crystal structure is rhombohedral or tetragonal. The tetragonal structure of the BFO (SG: *P*4*mm*) possesses P_s of around 150 μC/cm^2 along the [001] direction, and the rhombohedral structure (SG: *R*3*c*) possesses P_s of around 100 μC/cm^2 along the [111] direction without strain. [23,24] At the beginning of this research, in the case of bulk form, the

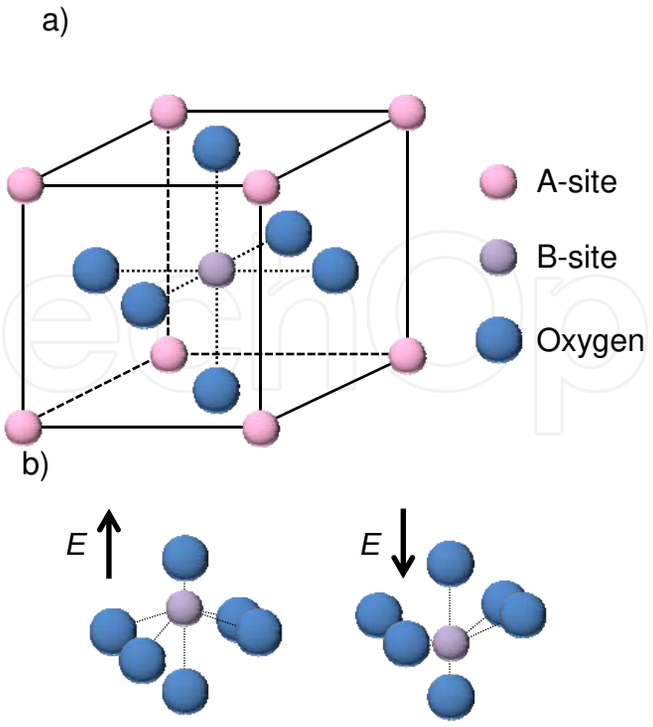

Figure 3. The crystal structure of typical perovskite-oxide: (a) The cubic phase, and (b) Schematic illustration of dipole switching with applying electric field $E>E_c$.

spontaneous polarization was 3.5 μC/cm² along the [001] direction, indicating a value of 6.1 μC/cm² along the [111] direction at 77 K. [25] Recently, it was reported that the bulk form of BFO showed P_s 60 μC/cm² along the [111] direction 9er, in thin-film BFO, large remanent polarizations ranging from 100 to 150 μC/cm² have been reported. [9,10] The difference between the thin-film and bulk values, initially attributed to epitaxial strain, could also result from mechanic constraints in granular bulk ceramics and from leakage effects in crystals caused by defect chemistry or the existence of second phases.

2.3. Fabrication method

2.3.1. Preparation method using chemical solution deposition

Chemical solution deposition (CSD) [26] is the method for fabrication of thin films using a precursor solution; several types of metal-organic compounds such as metal alkoxide and metal carboxylate compounds can be used as the precursor solution. The fabrication of thin films by this approach involves four basic steps:

i. Synthesis of the precursor solution;

ii. Deposition by spin-casting or dip-coating, where the drying processes usually depends on the solvent;

iii. Low-temperature heat treatment for drying, pyrolysis of organic species (typically 300–400°C), and formation of an amorphous film;

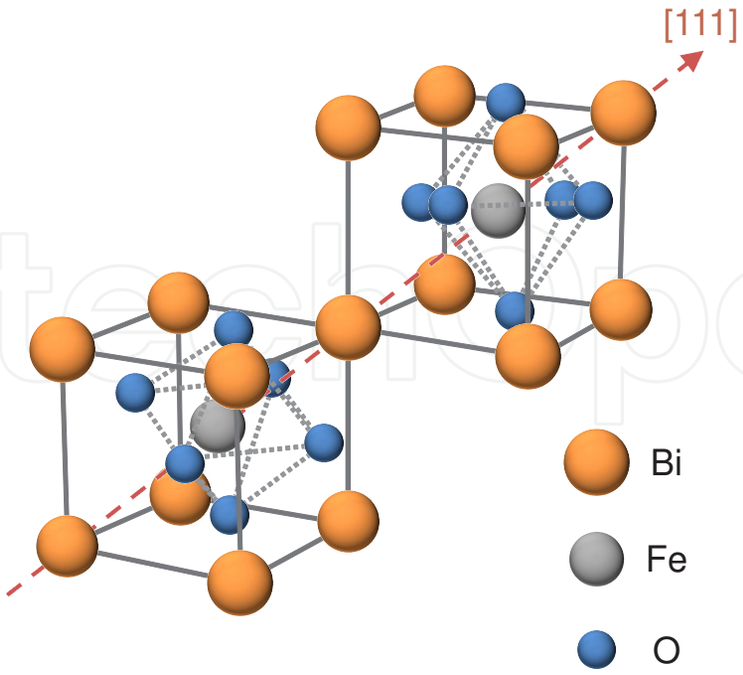

Figure 4. Schematic view of the *R*3*c* structure built up from two cubic perovskite $BiFeO_3$ unit cells. The cations are displaced along the [111] direction relative to the anions, and the oxygen octahedral rotate with alternating sense around the [111] axis.

iv. Higher-temperature heat treatment for densification and crystallization of the coating into the desired oxide phase (600–1100°C).

For most solution deposition approaches, the final three steps are similar despite differences in the characteristics of the precursor solution, and for electronic devices, spin-casting has been used almost exclusively. Depending on the solution route employed, different deposition and thermal processing conditions may be used for controlling film densification and crystallization in order to prepare materials with optimized properties.

For the fabrication of perovskite thin films, the most frequently used CSD approaches may be grouped into three categories:

i. Sol-gel processes that use 2-methoxyethanol as a reactant and solvent.

ii. Chelate processes that use modifying ligands such as acetic acid.

iii. Metal-organic decomposition (MOD) routes that use water-insensitive metal carboxylate compounds.

Other approaches that have also been used, although less extensively, include the nitrate method, citrate route, and Pechini process. In this study, a sol-gel solution and an enhanced-MOD (EMOD) solution (symmetric) were used because of their manageability.

2.3.2. Synthesis of the precursor solution for CSD

Processes based on 2-methoxyethanol are most appropriately considered sol-gel processes, and the key reactions leading to the formation of the precursor solutions are hydrolysis and condensation of the alkoxide reagents, in which metal-oxygen-metal (M-O-M) bonds are formed:

Hydrolysis:

$M(OR)_nH_2O \rightarrow M(OR)_{n-1}(OH)ROH.$

Condensation:

$M(OR)_nM(OR)_{n-1}(OH) \rightarrow M_2O(OR)_{2n-2}ROH.$

In some cases, an alcohol exchange reaction occurs in a practical synthesis process.

Alcohol exchange:

$M(OR)_nxR'OH \rightarrow M(OR)_{n-x}(OR')_xxROH.$

where OR is a reactive alkoxy group and OR' is the less reactive methoxyethoxy group.

In addition, to prepare a compound oxide material using two or more kinds of metal compounds in order to increase the homogeneity of the precursor solution, a double alkoxide with M-O-M'-O bonds may be synthesized for refluxing in an inactive gas atmosphere.

Synthesis of double alkoxide:

$xM(OR)_mM'(OR')_n \rightarrow xMM'(OR)_m(OR')_n$

In addition, if a metal alkoxide and carboxylate compounds are used, the synthesis is occasionally accompanied by an esterification reaction.

Esterification reaction:

$M(OR)_nM'(O_2CR')_m \rightarrow (OR)_{n-1}MOM'RO_2CR'(O_2CR')_{m-1}RO_2CR'$

For reproducible thin films, byproducts such as esters produced during the synthesis should be removed from the precursor solution through fraction distillation.

2.3.3. Preparation conditions of BFO polycrystalline films

The BFO films were formed through CSD. A precursor solution for CSD was prepared from bismuth acetate (99.99%, Aldrich), iron acetylacetonate (99.9%, Wako) in a solvent of 2-methoxyethanol (99.7%, Aldrich), and acetic acid (99.5%, Wako). The solution was heated to 80–100°C while stirring for 30 min to promote the dissolution of the precursors, followed by stirring at RT for 1 day before film deposition. The solution was synthesized on the basis of a stoichiometric composition. The concentration of the precursor solution was adjusted to be 0.05 M.

Figure 5 shows the process flow for the fabrication of the polycrystalline BFO film through CSD. A (111)Pt/Ti/SiO_2/(100)Si substrate was spin coated with the precursor solution at 3000

rpm for 30 s. The spin-coated film was dried at 150°C for 1 min and pyrolized at 400°C for 2 min in air. After the processes from spin coating to pyrolysis were repeated 10 times, the film was fired at 550°C for 5 min in air through rapid thermal annealing (RTA). This sequence was repeated 10 times. The film was polycrystalline with a random orientation and was approximately 650 nm thick.

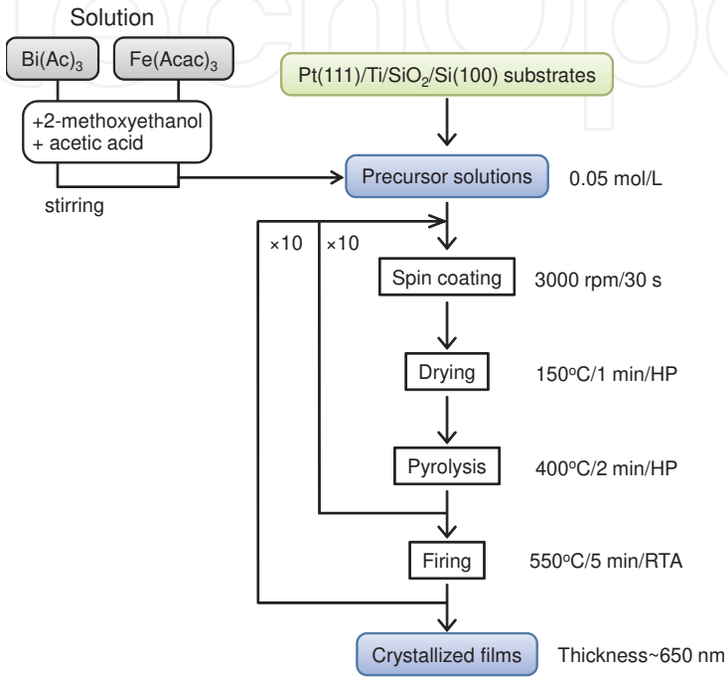

Figure 5. The process flow for fabrication of BFO films by CSD method.

2.4. Optical properties of ferroelectrics

2.4.1. Refractive index

The general definition of refractive index n is:

$$n = \frac{c_0}{v} \tag{1}$$

where c_0 is the speed of light in vacuum, and v, the speed of light in a material. The refractive index is related to the dielectric constant ε_r through the following equation:

$$\varepsilon_r = n^2 \tag{2}$$

This relationship is only valid when the interacting electric field has a frequency on the order of THz or higher and when the material is isotropic. The general behavior of condensed matter in an alternating electric field is that moving charges cause a frequency-dependent phase shift between the applied field and the electric displacement. Mathematically, this is expressed by writing the permittivity ε as a complex function:

$$\varepsilon(\varpi) = \varepsilon_1(\varpi) - i\varepsilon_2(\varpi) \tag{3}$$

The real part ε_1 characterizes the electric displacement, and the imaginary part ε_2 denotes the dielectric losses. The loss tangent is defined as

$$\tan\delta = \frac{\varepsilon_2}{\varepsilon_1} \tag{4}$$

Since light is an alternating electromagnetic wave with the electric and magnetic field vibration directions perpendicular to one another, the electric field induces an electric polarization in a dielectric crystal and the light itself is influenced by the crystal. The alternating frequency of light is so high (λ= 500 nm corresponds to a frequency of approximately 600 THz) that only electronic polarization can follow the electric field change. Therefore, the relative permittivity of an optically transparent crystal is small, typically less than 10. It is known that a dielectric material shows wavelength dispersion of its refractive index at optical frequencies.

2.4.2. Optical indicatrix and anisotropy of refractive index

In a microscopically anisotropic medium, the refractive index is generally different for different crystal directions. Ferroelectric materials, particularly in film form, can be both optically isotropic and optically anisotropic. Ferroelectric ceramics or polycrystalline films are an example of the former type; their isotropic behavior is due to the random orientation of their constituent grains. Ferroelectric single crystals or epitaxial films are an example of the latter type, and they can be divided into optically uniaxial and optically biaxial crystals. If a coordinate system is chosen to coincide with the three principal axes of a crystal, we have the following relations:

$$\varepsilon_x = n_x^{\,2}, \quad \varepsilon_y = n_y^{\,2}, \quad \varepsilon_z = n_z^{\,2}. \tag{5}$$

The optical anisotropy of a crystal is characterized by an optical indicatrix (or index ellipsoid) defined as

$$\frac{x^2}{n_x^{\,2}} + \frac{y^2}{n_y^{\,2}} + \frac{z^2}{n_z^{\,2}} = 1, \tag{6}$$

where n_x, n_y, and n_z are the principal refractive indexes, as shown in Fig. 2.6. The optical indicatrix is mainly used to find the two refractive indexes associated with the two independent plane waves that can propagate along an arbitrary direction k in a crystal. The optical indicatrix is used as follows: The intersection ellipse between the optical indicatrix and a plane through the origin point normal to the propagation direction k is found. The two axes of the intersection ellipse are equal in length to $2n_1$ and $2n_2$, where n_1 and n_2 are the two refractive indexes.

In the case of a biaxial crystal, there are two optical axes, and the refractive indexes are different in all three principal directions, $n_x \neq n_y \neq n_z$. In the common case of a uniaxial crystal, we have $n_x = n_y = n_o$ and $n_z = n_e$, where n_o and n_e are the ordinary and extraordinary refractive indexes, respectively. The refractive index along the optical axis corresponds to the extraordinary index n_e, and the refractive index perpendicular to the optical axis corresponds to the ordinary index n_o, as shown in Fig. 6. The existence of two rays with different refractive indexes is called birefringence. The birefringence Δn is usually defined as:

$$\Delta n = n_e - n_o \tag{7}$$

Since the value of n_e may be either higher or lower than n_o, birefringence may take on positive or negative values. If $\Delta n > 0$, the crystal is said to be optically positive, whereas if $\Delta n < 0$, it is said to be optically negative. For light propagating in a different direction from the principal axis in a uniaxial crystal, the situation becomes more complicated. A light wave with the wave vector κ, as shown in Fig. 6, has a constant ordinary index, whereas the extraordinary refractive index is dependent on the angle θ as:

$$\frac{1}{n_e(\theta)^2} = \frac{\cos^2\theta}{n_o^{\,2}} + \frac{\sin^2\theta}{n_e^{\,2}}. \tag{8}$$

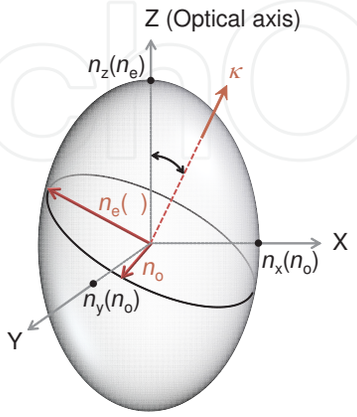

Figure 6. Schematic view of the *R*3*c* structure built up from two cubic perovskite $BiFeO_3$ unit cells. The cations are displaced along the [111] direction relative to the anions, and the oxygen octahedral rotate with alternating sense around the [111] axis.

2.4.3. Thermooptic effect

The thermo-optic effect refers to thermal modulation of the refractive index of a material. The refractive index of a material can be modulated as a function of its thermooptic coefficient α as

$$n(T) = n_0 - \alpha \cdot T, \tag{9}$$

where T is the temperature and $n(T)$ and n_0 are the refractive indexes at an arbitrary temperature and at 0°C, respectively. The thermo-optic coefficient relates the changes in the optical indicatrix ΔB_{ij} with the changes in temperature ΔT. Since temperature is a scalar, the thermo-optic effect is a symmetric second-rank tensor similar to the dielectric constant. The temperature dependence of the refractive index is generally small, except near phase transformations. The situation is analogous to low-frequency dielectrics. For silica and alumina, the permittivity is nearly independent of temperature, but ferroelectrics exhibit enormous changes near T_c. The refractive index of common oxides increases with density. Because of thermal expansion, density decreases with increasing temperature, thus decreasing the refractive index as well. Thermal expansion makes a small negative contribution to the temperature coefficient of refractive index dn/dT. This effect is often influenced by changes in the electronic band gap or by phase changes. These effects can be either positive or negative, depending on the nature of the energy levels or on the location of the phase transformation.

2.5. Evaluation method of optical properties

Spectroscopic ellipsometry

Ellipsometry determines the optical constants and thickness of materials in layered samples by fitting a parameterized model to the measured data for simultaneously analyzing data from multiple samples. Figure 7 shows a schematic illustration of ellipsometry. The linearly polarized incident light is reflected after interacting with the sample. The polarization of the light changes from linear to ellipsoidal from this interaction. We measure the polarization state using the ratio of the reflection coefficients for the light polarized parallel (p) and perpendicular (s) to the plane of incidence. This ratio, called the ellipsometric parameter, is defined as [27-30]

$$\rho = \frac{R_p}{R_s} = \tan(\psi)\exp(i\Delta), \tag{10}$$

where R_p and R_s are the Fresnel reflection coefficients of polarized light parallel and perpendicular to the incident plane, respectively. Here, tan (ψ) and Δ are the amplitude and phase of ρ, respectively. The Fresnel reflection coefficients are represented as follows:

For p-polarized light,

$$R_p = \frac{\tilde{n}^2 \cos\varphi - \sqrt{\tilde{n}^2 - \sin^2\varphi}}{\tilde{n}^2 \cos\varphi + \sqrt{\tilde{n}^2 - \sin^2\varphi}}, \tag{11}$$

and for *s*-polarized light,

$$R_s = \frac{\cos\varphi - \sqrt{\tilde{n}^2 - \sin^2\varphi}}{\cos\varphi + \sqrt{\tilde{n}^2 - \sin^2\varphi}}. \tag{12}$$

Here, ñ is the complex refractive index, and Φ, the incident angle.

In this study, a Gaussian oscillator was used to model a dielectric function to represent film properties. Gaussian oscillators represent the normal distribution for the ε_2 spectrum; the ε_1 spectrum is determined by the ε_2 values because the Kramers-Kronig (KK) relation couples the real and imaginary parts of the complex dielectric constant. When a Gaussian oscillator is used as a dielectric function, complex dielectric constants (ε_1, ε_2) are calculated as [31,32]

$$\varepsilon_2 = A_n \exp\left[-\left(\frac{E - E_n}{B_n}\right)\right] + A_n \exp\left[-\left(\frac{E + E_n}{B_n}\right)\right], \tag{13}$$

$$\varepsilon_1 = 1 + \frac{2}{\pi} P \int_0^\infty \frac{\xi \varepsilon_2(\xi)}{\xi^2 - E^2} d\xi, \tag{14}$$

where A_n is the amplitude of the oscillator; E_n, the central energy of the oscillator; B_n, the broadening of the oscillator; and P, Cauchy's principal value. Optical constants (n, k) are equivalent to the complex dielectric constants (ε_1, ε_2). Therefore, optical constants (n, k) can be determined from the Gaussian oscillator parameters, which show the best fitting for experimental values of Φ and Δ. Model fitting was carried out by minimizing the mean square error (MSE) function defined as [27,29]

$$\mathrm{MSE} = \frac{1}{2N - M} \sum_{i=1}^{N} \left[\left(\frac{\psi_i^{\mathrm{mod}} - \psi_i^{\mathrm{exp}}}{\sigma_{\psi_i}^{\mathrm{exp}}} \right)^2 + \left(\frac{\Delta_i^{\mathrm{mod}} - \Delta_i^{\mathrm{exp}}}{\sigma_{\Delta_i}^{\mathrm{exp}}} \right)^2 \right], \tag{15}$$

where N is the number of (ψ, Δ) pairs, M is the number of variable parameters in the model, σ is the standard deviation on the experimental points, and the superscripts "mod" and "exp" represent the calculated and experimental values, respectively.

http://dx.doi.org/10.5772/54908

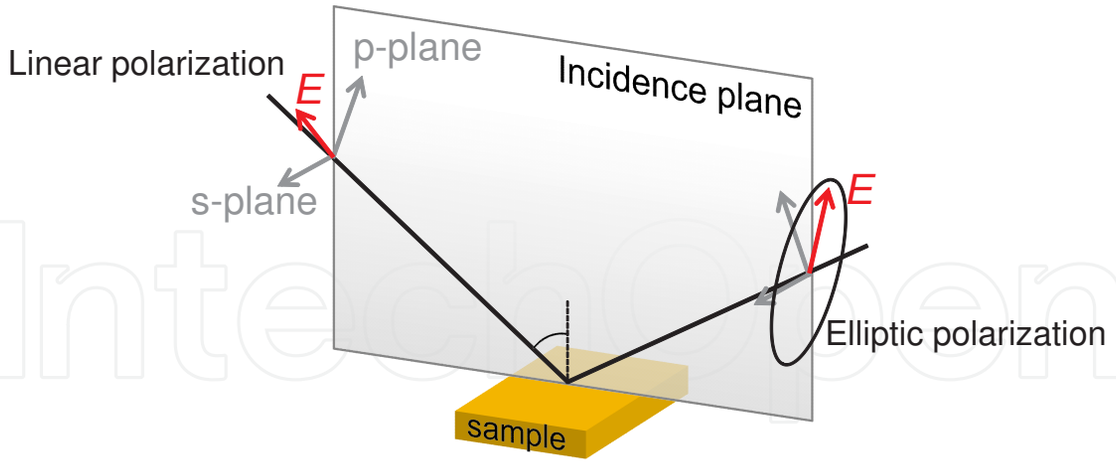

Figure 7. Schematic illustration of the ellipsometry.

3. Optical properties of multiferroic $BiFeO_3$ films

3.1. Fundamentals

Multiferroic materials, which simultaneously exhibit ferroelectricity and magnetic ordering, have attracted considerable attention, not only in terms of scientific interest but also because of their potential applications in novel functional devices. BFO is one of the few materials that exhibit dielectric and magnetic ordering at room temperature. [17,18] BFO also exhibits a large remanent polarization of 100 $\mu C/cm^2$ in thin film form. [9,10] Therefore, the electric and magnetic properties of BFO films have been the subject of intense research in recent years. [11-13] However, few reports on their optical properties [14,15] or their applications [16] have been published. It is important to know the exact optical properties of BFO films in order to develop various optical applications. To apply BFO films to optical devices, the electro-optic, magneto-optic, and thermo-optic effects of the films can be controlled by modulating their refractive indices. Recently, a Mach-Zehnder-type optical switch, which employs the thermo-optic effect, is a topic of immense interest in the photonics field. [33-35] In this section, we examine the optical constant and the temperature dependence of the refractive index of polycrystalline BFO films.

3.2. Experimental machines

- Crystal structure and orientation: X-ray diffractometer (PANalytical, X'pert PRO MPD)
- Morphology: field emission scanning electron microscope (JEOL, JIB-4500FE), transmission electron microscope (Hitachi, HF-2000), atomic force microscope (SII, SPI3800N)
- Electrical property: ferroelectric test system (Toyo, FCE)
- Optical property: spectroscopic ellipsometer (J. A. Woollam, M-2000) with a heating stage, as shown in Fig. 8(a) and 8(b).

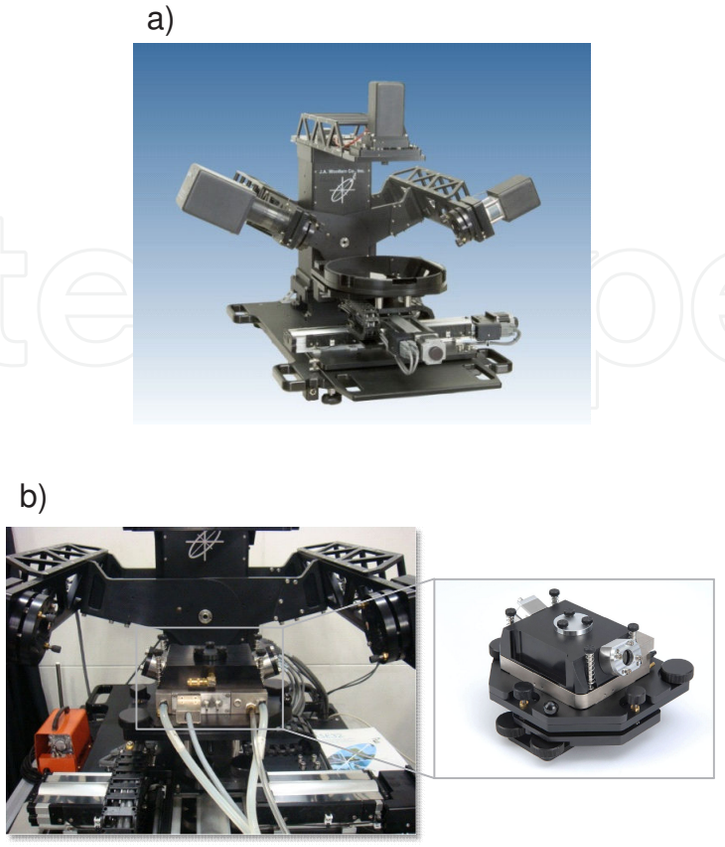

Figure 8. (a) Spectroscopic ellipsometer (J. A. Woollam, M-2000) used in this study, and (b) the heating stage used for annealing sample from RT to 600°C.

3.3. Fundamental properties of polycrystalline BFO film

Polycrystalline BFO films were successfully formed on the Pt/Ti/SiO_2/Si substrates through CSD. Figure 9 shows the XRD θ-2θ pattern of the polycrystalline BFO film. The XRD analysis, it was confirmed that the BFO film was crystallized into a single perovskite phase with a random orientation.

Figure 10 shows the *P-E* hysteresis loop of the polycrystalline BFO film, measured with a single triangular pulse of 100 kHz at room temperature. From this figure, the ferroelectricity of the film can be confirmed. By a positive-up-negative-down (PUND) measurement technique [36] using a pulse train with an amplitude of 1.53 MV/cm and a width of 5 μs, a remanent polarization of 30 μC/cm^2, relative permittivity of 280, and leakage current density of 7.6 A/cm^2 were estimated at room temperature.

Figure 11 shows a) the surface morphology and the cross-sectional images of (b) the cleavage face and (c) the worked surface using a focused ion beam. From Fig. 11(a) and (b), it can be seen that the polycrystalline BFO film consists of small randomly grown grains, whereas the bottom Pt layer has a columnar grain growth. From Fig. 11(c), voids in the film were confirmed. Film thickness was estimated to be approximately 650 nm from cross-sectional images.

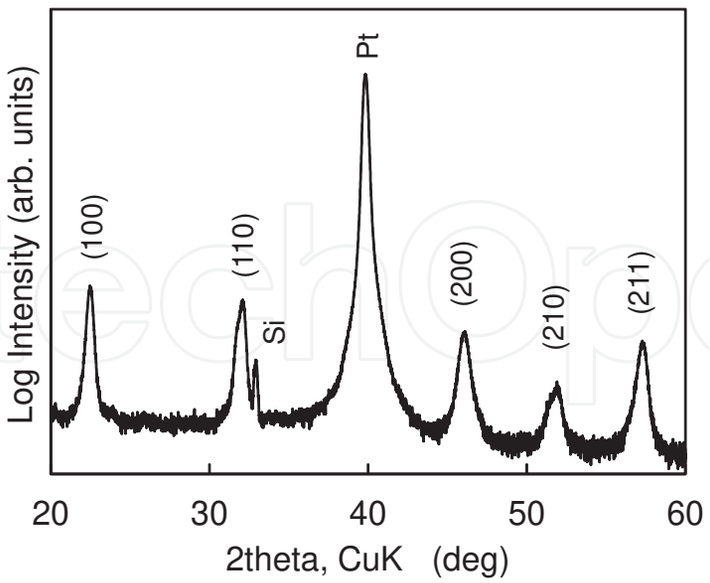

Figure 9. The XRD θ-2θ pattern of the polycrystalline BFO film.

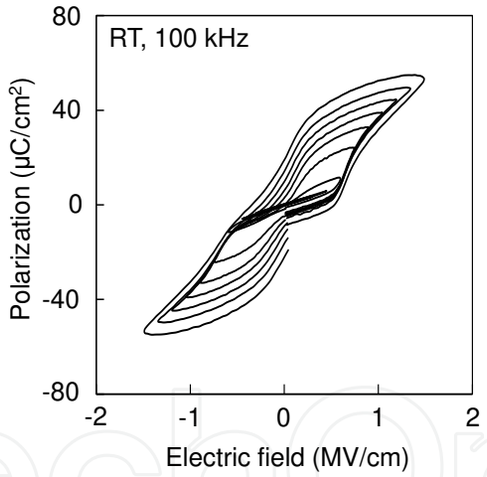

Figure 10. The *P-E* hysteresis loop of the polycrystalline BFO film measured with a single triangular pulse of 100 kHz at room temperature.

3.4. Optical constants of polycrystalline BFO film

Ellipsometric spectra in (Δ, ψ) were recorded at tincident angles of θ_i = 50°, 60°, and 70° in a spectral range of 245–1670 nm. Figure 12 shows the multilayer model used in this study. It was assumed that the model consisted of ambient (air), a surface layer, a bulk layer, and a substrate (Pt). The optical constants of the surface layer were represented by the Bruggeman effective medium approximation (EMA) [37] consisting of a 0.50 bulk film/0.50 void mixture. In the polycrystalline BFO film, 4 Gaussian oscillators were assumed to represent the film properties.

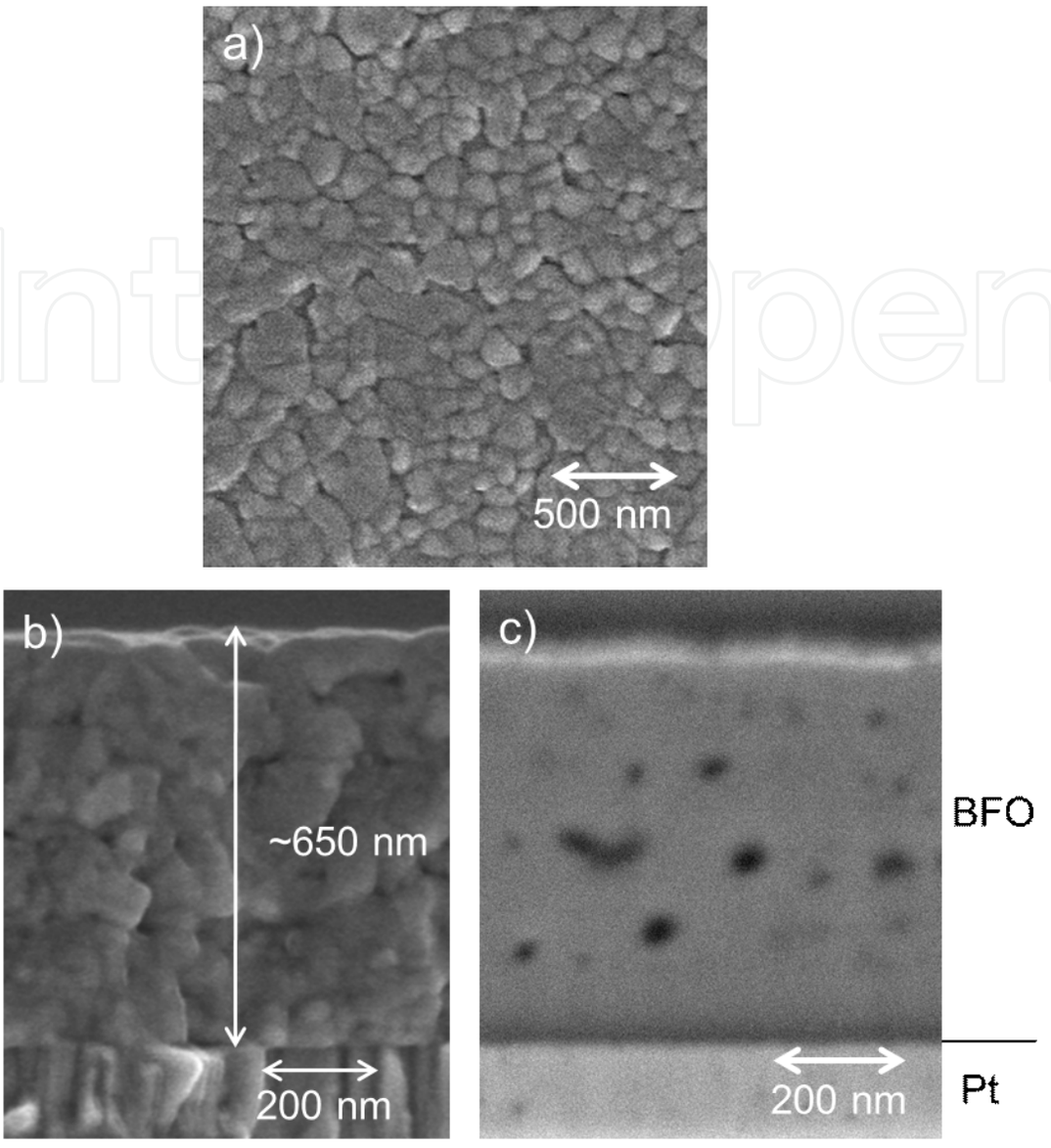

Figure 11. (a) The surface morphology and the cross-sectional images of (b) cleavage face and (c) worked surface by focused ion beam.

Furthermore, the density gradient along the film thickness, which affects the refractive index gradient, was also introduced by applying the EMA. Figure 13(a)–(d) shows the ψ and Δ spectra of the polycrystalline BFO film measured at various incident angles and fitting curves. The fitting parameters are summarized in Table 1. Figure 13(a) and (b) shows the results without the assumption of the refractive index gradient. In this case, the fitting curve did not represent the experimental result well and the MSE was relatively large. Figure 13(c) and (d) shows that when the refractive index gradient was considered, the MSE decreased from 106.6 to 66.6, and the fitting curves represented the experimental results well. This refractive index gradient seems to be caused by the distribution of voids in the film, as shown in Fig. 11(c). The total thickness of the polycrystalline BFO film was estimated to be approximately 650 nm. This value coincided with that observed in the cross-sectional SEM image shown in Fig. 11(a).

Figure 14 shows the optical constant of the polycrystalline BFO film in the wavelength range of 245 - 1670 nm calculated from the best-fitting results. In Fig. 14, the solid and broken lines represent the maximum and minimum values, respectively, of each optical constant in the graded layer. A large refractive index of 3.22 was estimated for the polycrystalline BFO film; this value is higher than that of rutile-type TiO_2 film, which has the highest refractive index among oxides reported thus far. At a wavelength of 600 nm, the refractive index of our BFO film was 3.22 and that of the TiO_2 film was reported to be approximately 2.6. [38] Figure 15 shows the depth profile of the refractive index and the extinction coefficient of the BFO film at a wavelength of 500 nm. This profile shows that the refractive index near the substrate is larger than that at the surface area. The reason for this gradient is not yet clear, although one possible explanation is the existence of voids in the film.

To determine the optical band gap, we plot $(\alpha E)^2$ vs. E for the polycrystalline BFO film, as shown in Fig. 16(a), where α and E are the absorption coefficient and photon energy, respectively. The absorption coefficient α is given by

$$\alpha = \frac{4\pi k}{\lambda}, \tag{16}$$

where k is the extinction coefficient and λ, is the wavelength. A good linear fit above the band gap indicates that the BFO film has a direct gap. [15] The linear extrapolation of $(\alpha E)^2$ to 0 induces band gaps of 2.79 eV for the polycrystalline BFO film. This means that the absorption edge of the BFO film is 445 nm. This value for the polycrystalline BFO film was similar to that in recent reports. [15,39,40] Next, we plot $(\alpha E)^{1/2}$ vs. E in Fig. 16(b) for the BFO film. The $(\alpha E)^{1/2}$ vs. E plot did not show 2 clear slopes as was expected for an indirect gap material. [41] Finally, the polycrystalline BFO film was found to show a sufficiently low light loss at a wavelength greater than 600 nm so that its large reflective index at visible wavelengths is useful for electric-optic devices such as an electro-optic spatial light modulator.

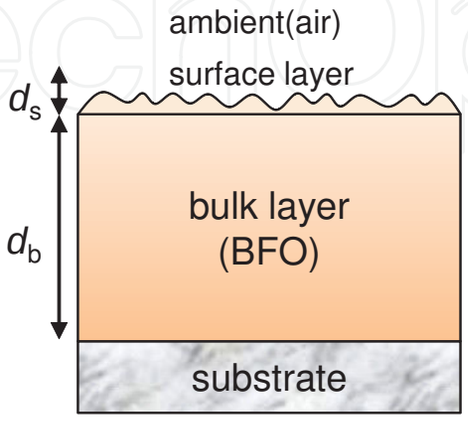

Figure 12. A multilayer model used in this study.

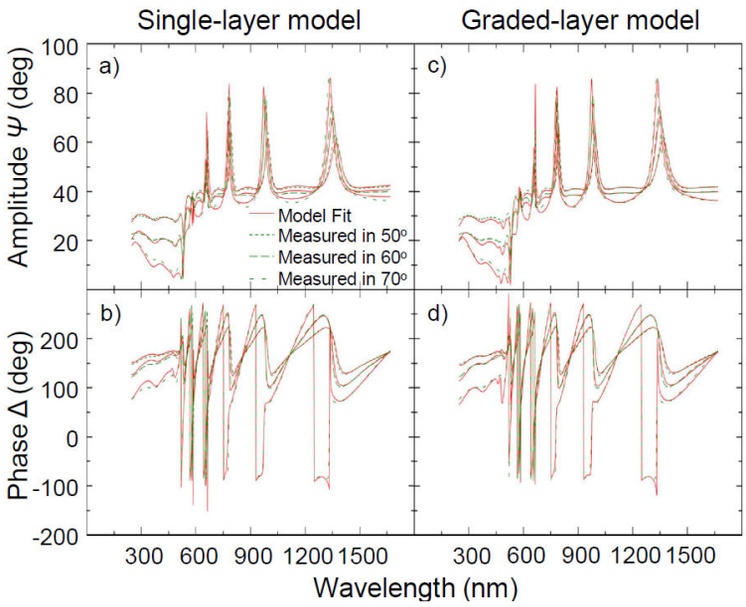

Figure 13. Ψ and Δ spectra of the polycrystalline BFO film measured at various incident angles and fitting curves obtained using the model (a) - (b) without and (c) - (d) with refractive index gradient.

$$\varepsilon_1 = 1 + \frac{2}{\pi} P \int_0^{\infty} \frac{\xi \varepsilon_2(\xi)}{\xi^2 - E^2} d\xi, \quad \varepsilon_2 = A_n \exp\left[-\left(\frac{E - E_n}{B_n}\right)\right] + A_n \exp\left[-\left(\frac{E + E_n}{B_n}\right)\right]$$

Fitting parameters		Sample-Model	
		BFO-single	BFO-graded
Thickness (nm)	d_s	3.566±0.635	4.597±0.224
	d_b	667.423±3.31	644.839±1.92
Amplitude A_n	A_{n1}	6.771	9.834
	A_{n2}	8.981	10.973
	A_{n3}	3.638	5.008
	A_{n4}	0.735	0.716
Central energy E_n (eV)	E_{n1}	4.175	4.119
	E_{n2}	7.460	7.348
	E_{n3}	3.024	3.052
	E_{n4}	2.491	2.476
Broadening B_n (eV)	B_{n1}	1.201	1.205
	B_{n2}	4.254	4.254
	B_{n3}	0.527	0.527
	B_{n4}	0.215	0.215
MSE		106.6	66.66

Table 1. The fitting parameters in single layer model and graded layer model of the polycrystalline BFO films. Gaussian oscillator defined as following equation.

http://dx.doi.org/10.5772/54908

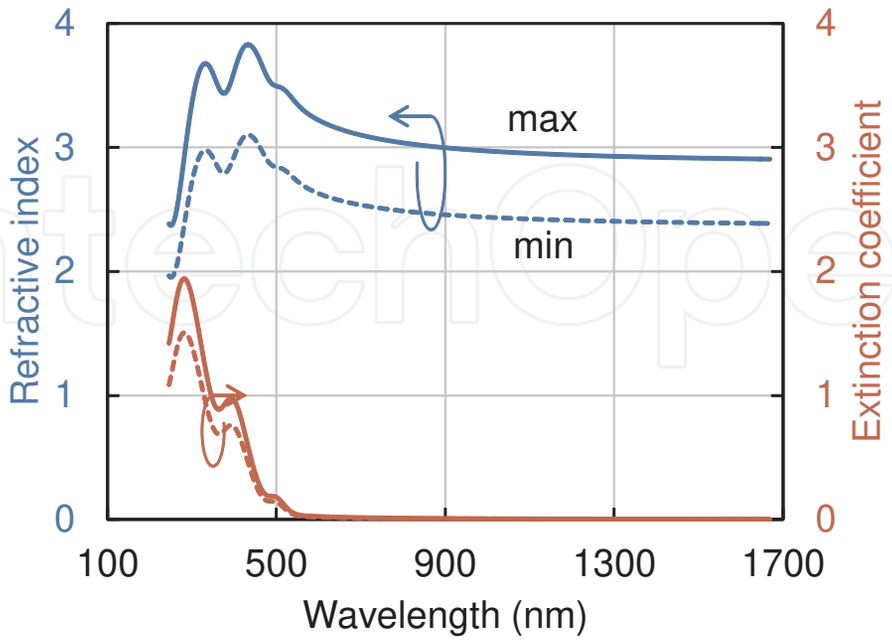

Figure 14. Refractive index and extinction coefficient of the polycrystalline BFO film; the solid and broken lines show maximum and minimum values, respectively.

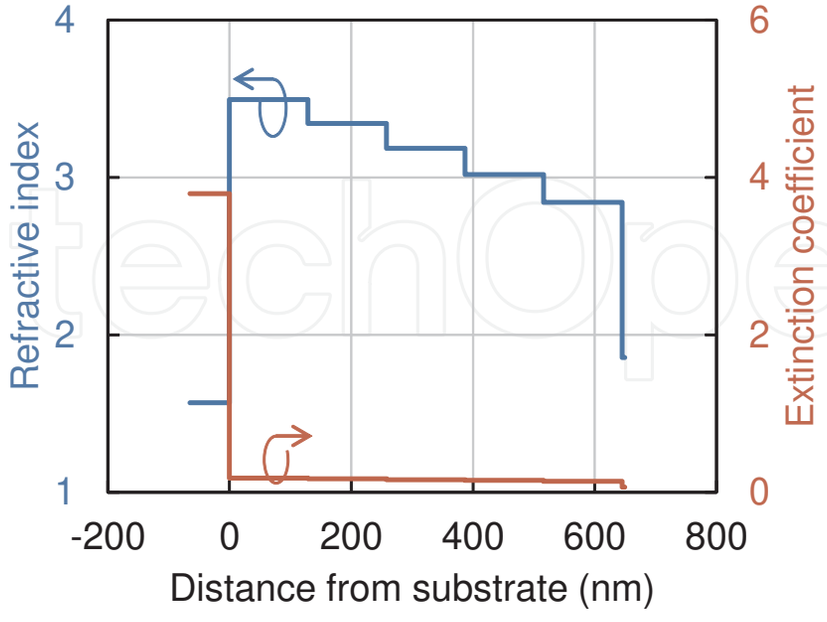

Figure 15. Depth profile of refractive index and extinction coefficient of the BFO film at a wavelength of 500 nm.

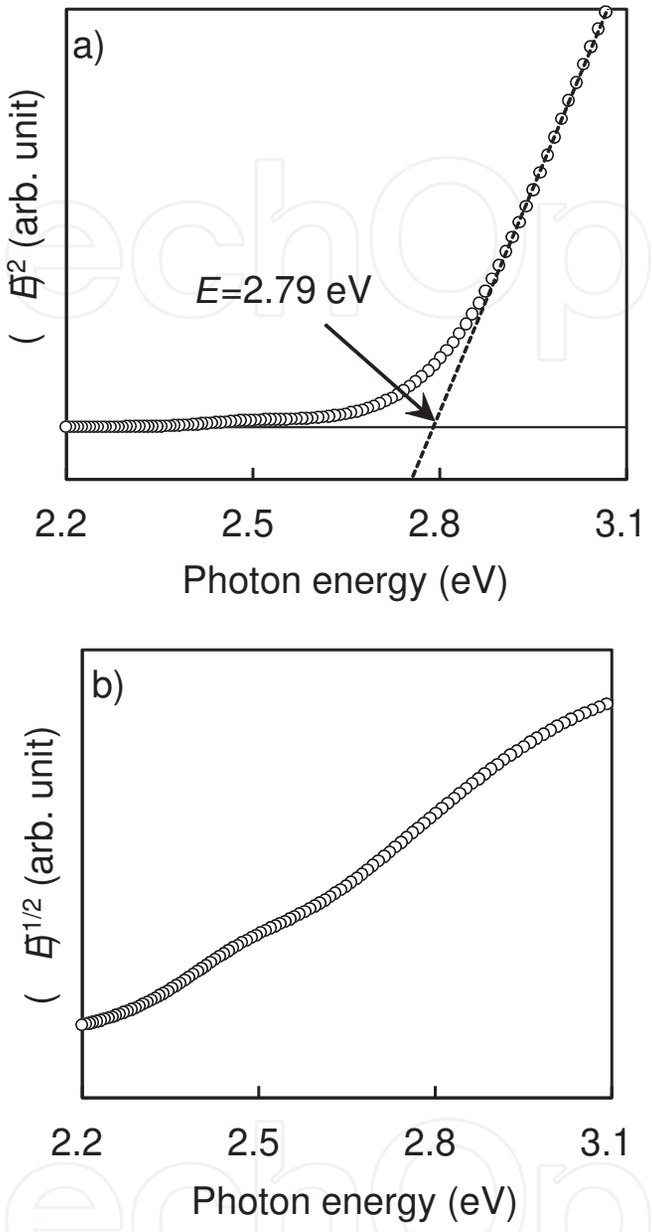

Figure 16. Plots of (a) $(\alpha E)^2$ and (b) $(\alpha E)^{1/2}$ vs. photon energy E for the polycrystalline BFO film. The linear extrapolation of $(\alpha E)^2$ to 0 gives band gaps of 2.79 eV.

3.5. Thermooptic property of polycrystalline BFO film

3.5.1. Temperature dependence of lattice space

Figure 17 shows the lattice spacing of Si (400), BFO (100), and Pt (111) as a function of temperature, estimated from XRD patterns. All the *d*-spaces monotonically increased with

http://dx.doi.org/10.5772/54908

increasing temperature because of thermal expansion. Thermal expansion coefficients, estimated from Fig. 17, are shown in Table 2, which includes reference data [42-44] for comparison. From this table, we can see that our experimental values are larger than those in reference data, except for the Si substrate because of the effect of in-plane compressive stress.

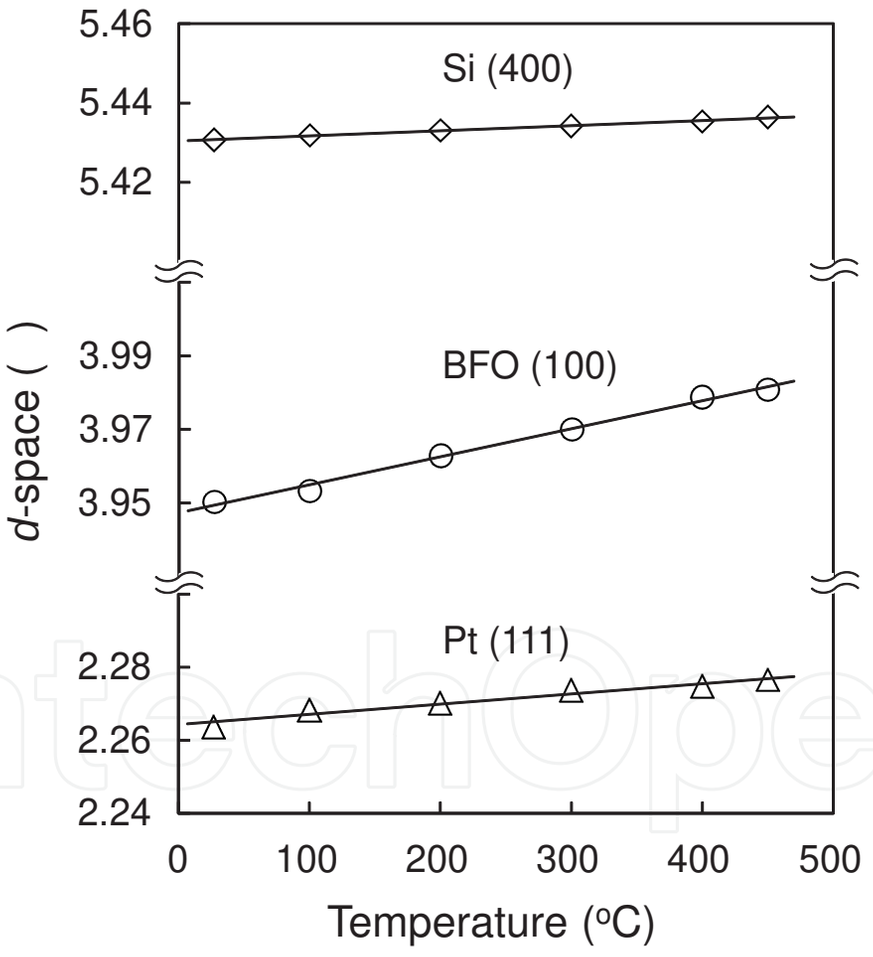

Figure 17. The lattice spacing of Si (400), BFO (012), and Pt (111) as a function of temperature estimated from XRD patterns.

Material	Thermal expansion coefficient	
	Experimental data ($\times 10^{-6}$ K^{-1})	Reference data ($\times 10^{-6}$ K^{-1})
BFO	19	10-14
Pt	12	9
Si	2.4	2

Table 2. The thermal expansion coefficients of the BFO, Pt, and Si.

3.5.2. Temperature dependence of refractive index

Ellipsometric spectra in (Δ, Ψ) were recorded at incident angles of $\theta_i = 70^o$ in a spectral range of 245–1670 nm. The sample was loaded onto the customized heating stage and heated from RT to 530°C. In these measurements, one Gaussian oscillator was assumed to represent film properties, and the central energy E_n of the oscillator was fixed at 5 eV for each temperature. Figure 18(a) – b) shows the wavelength dispersion of the refractive index and the extinction coefficient measured at 50 and 530°C, respectively. From this figure, we observe that the refractive index decreases with increasing temperature for all wavelengths. The refractive index variation with increasing temperature is large for shorter wavelengths. Based on these results, we investigated the origin of the temperature dependence of refractive index dispersion, as shown in Fig. 18. In the short-wavelength region, the lattice vibration becomes more intense with increasing temperature; therefore, in a high-temperature region, the amplitude of the oscillator decreased, and the broadening of the oscillator expanded. At the same time, density is decreased with increasing temperature owing to thermal expansion; therefore, the refractive index decreased in all wavelength regions. This combination seems to be responsible for the refractive index curve shown in Fig. 18(a).

Figure 19 shows the temperature dependence of the refractive index in a long- wavelength region. It is found that refractive index decreases with increasing temperature at each wavelength, although there was some variability. The thermo-optic coefficient was estimated from the slopes of linear approximation. A thermo-optic coefficient of 0.8×10^{-4} K^{-1} was obtained at a wavelength of 1550 nm for the BFO film. The thermo-optic coefficients of polymers and glasses, which are known to be typical thermo-optic materials, have been reported to be approximately 2×10^{-4} K^{-1} and 0.1×10^{-4} K^{-1}, respectively. [45,46] It is found that the BFO film shows a large refractive index and a thermo-optic coefficient comparable to that of these traditional materials. Finally, it can be concluded that the BFO also has potential for use in an electro-optic-type Mach-Zehnder modulator.

http://dx.doi.org/10.5772/54908

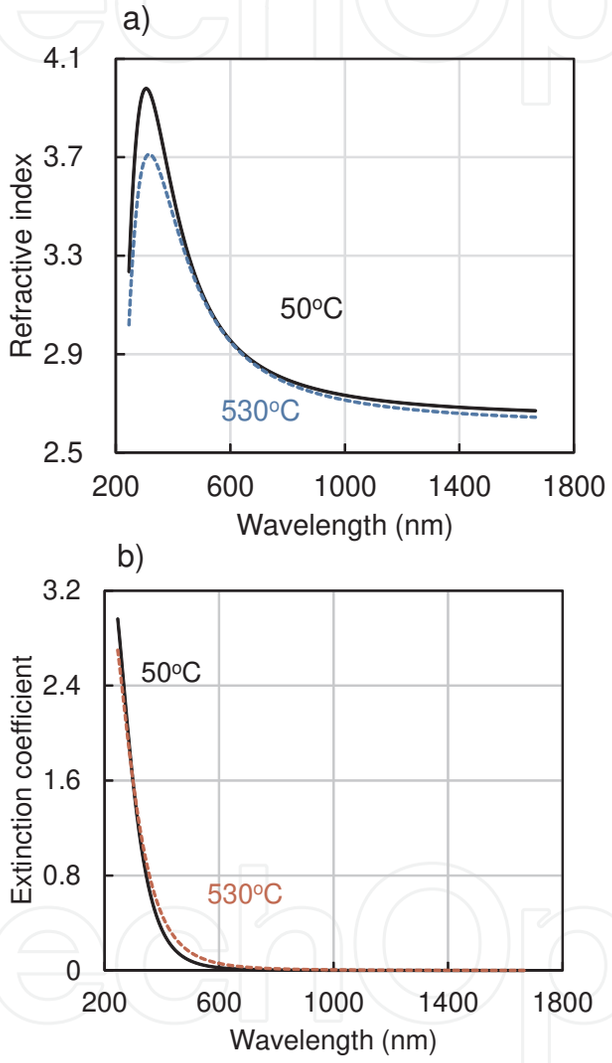

Figure 18. The wavelength dispersion of a) refractive index and b) extinction coefficient measured at 50 and 600°C, respectively.

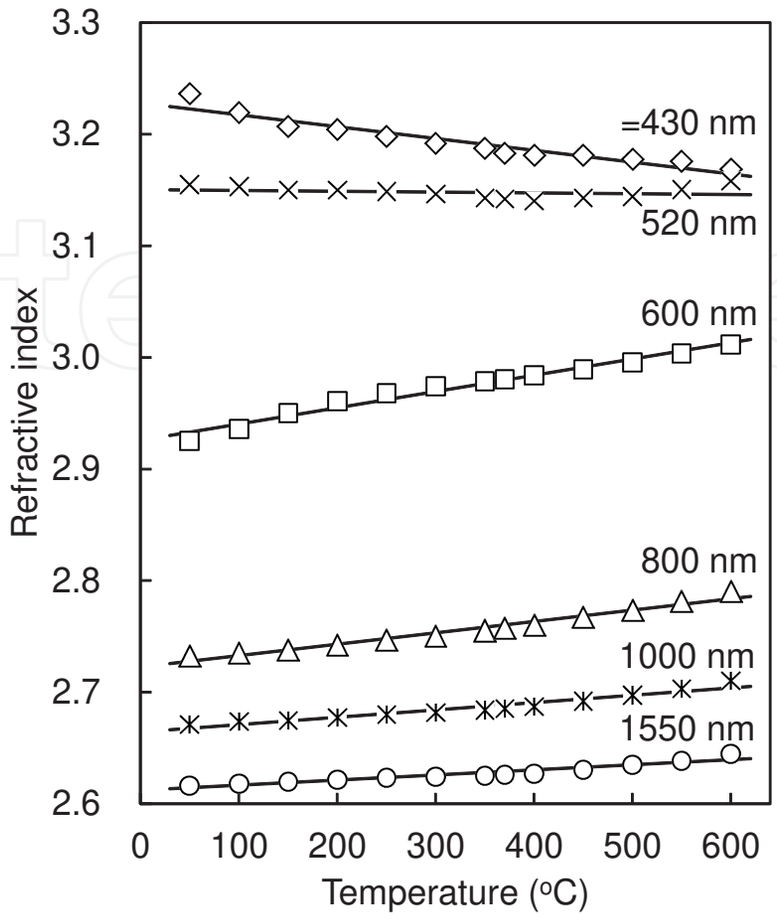

Figure 19. The refractive indexes at various wavelengths as a function of temperature.

4. Conclusions

The optical and thermo-optic properties of $BiFeO_3$ (BFO) films were studied. Polycrystalline BFO films were formed on $Pt/Ti/SiO_2/Si$ substrates, and their basic optical and thermo-optic properties were systematically evaluated. The new findings are summarized as follows:

i. The polycrystalline BFO films were evaluated using a spectroscopic ellipsometer. Gaussian oscillators were assumed as a dielectric function to represent film properties, and the graded model was assumed by introducing a refractive index gradient. As a result, large refractive indexes of 3.22 and 2.91 were estimated for the polycrystalline BFO film at wavelengths of 600 and 1550 nm, respectively, these refractive indexes are higher than that of the rutile-type TiO_2 film, which is known to have a high refractive index. The optical band gap of the BFO film at RT was estimated as a direct transition to be 2.79 eV, which corresponds to the absorption edge of 445 nm. It was found that the BFO film shows sufficiently low light loss at wavelengths larger than 600 nm.

ii. The thermo-optic properties of the BFO films were evaluated using a spectroscopic ellipsometer with a heating stage. The refractive index of the polycrystalline film decreased with increasing temperature. We considered that this change in refractive index is caused by the balance between the increase in refractive index due to the enhancement of the oscillator dispersion and the decrease in refractive index due to the decreased density of the film. In addition, we obtained thermo-optic coefficient of 0.8×10^{-4} K^{-1} at a wavelength of 1550 nm for the BFO film, which is larger than those of typical thermo-optic polymers (2×10^{-4} K^{-1}) and glasses (0.1×10^{-4} K^{-1}).

These results suggested that the BFO films have a high potential for application as an optical material with a high refractive index, and that the effectual refractive index change can be controlled by the balance of two factors, the activation of the oscillator and the thermal expansion coefficient, even in the same material.

Acknowledgements

The author thanks Assistant Prof. Takashi Nakajima, Tokyo University of Science, Prof. Akiharu Morimoto, Asso. Prof. Takeshi Kawae, Kanazawa University, Prof. Takashi Yamamoto, Ass. Prof. Ken Nishida, National Defense Academy, Dr. Takashi Iijima, AIST, Dr. Koichi Tsutsumi, Dr. Masahiro Matsuda, Dr. Michio Suzuki, J. A. Woollam Japan, and Dr. Toshiyasu Tadokoro Techno-Synergy, Inc. This study was partially supported by a Grant-in-Aid for JSPS Research Fellows (No. 217990) from the Japan Society for the Promotion of Science.

Author details

Hiromi Shima[1*], Hiroshi Naganuma[2*] and Soichiro Okamura[1]

*Address all correspondence to: shima@nda.ac.jp, naganuma@mlab.apph.tohoku.ac.jp

1 Department of Applied Physics, Tokyo University of Science, 1-3, kagurazaka, Shinjuku-ku, Tokyo, Japan

2 Department of Applied Physics, Graduate school of Engineering, Tohoku University, Japan

References

[1] Fujimori, Y.; Fujii, T.; Suzuki, T.; Kimura, H.; Fuchikami, T.; Nakamura, T.; and Takasu, H. (2005) *IEDM Tech. Dig.*, 2005 p.p. 935.

[2] Bitou, Y.; and Minemoto, T. (1998) High-contrast spatial light modulator by use of the electroabsorption and the electro-optic effects in a GaAs single crystal, *Appl. Opt.*, Vol. 37, August 1998, pp. 4347-4356.

[3] Thapliya, R.; Okano, Y.; and Nakamura, S. (2003) Electrooptic Characteristics of Thin-Film PLZT Waveguide Using Ridge-Type Mach–Zehnder Modulator, *J. Lightwave Tech.*, Vol. 21, January 2003 pp. 1820-1827.

[4] Jacobsen, R. S.; Andersen, K. N.; Borel, P. I.; Pedersen, J. F.; Frandsen, L. H.; Hansen, O.; Kristensen, M.; Lavrinenko, A. V.; Moulin, G.; Ou, H.; Peucheret, C.; Zsigri, B.; and Bjarklev, A. (2006) Strained silicon as a new electro-optic material, *Nature*, Vol. 441, May 2006 pp. 199-202.

[5] Shimizu, T.; Nakada, M.; Tsuda, H.; Miyazaki, H.; Akedo, J.; and Ohashi, K. (2009) Gigahertz-rate optical modulation on Mach-Zehnder PLZT electro-optic modulators formed on silicon substrates by aerosol deposition, *IEICE Electro. Exp.*, Vol. 6, December 2009 pp. 1669-1675.

[6] Xie, N.; Hashimoto.; T and Utaka, K. (2009) Very Low-Power, Polarization-Independent, and High-Speed Polymer Thermooptic Switch *IEEE Photonics Tech. Lett.*, Vol. 21, December 2009 pp. 1861-1863.

[7] Reed, G. T.; Mashanovich, G.; Gardes, F. Y.; and Thomson, D. J.; (2010) Silicon optical modulators, *Nature Photonics*, Vol. 4, July 2010 pp. 518-526.

[8] Haertling, G. H,; and Land, C. E.; (1971) Hot-Pressed (Pb, La)(Zr,Ti)O_3, Ferroelectric Ceramics for Electrooptic Applications*J. Am. Ceram. Soc.*, Vol. 54, October 1971, pp. 1-11.

[9] Wang, J.; Neaton, J. B.; Zheng, H.; Nagarajan, V.; S. Ogale, B.; Liu, B.; Viehland, D.; Vaithyanathan, V.; Schlom, D. G.; Waghmare, U. V.; Spaldin, N. A.; Rabe, K. M.; Wuttig, M. & Ramesh, R. (2003) Epitaxial $BiFeO_3$ Multiferroic Thin Film Heterostructures, *Science* Vol. 299, February 2003, pp. 1719-1722.

[10] Yun, K. Y.; Rincinschi, D.; Kanashima, T.; Noda, M.; and Okuyama, M.; (2004) Giant Ferroelectric Polarization Beyond 150 μC/cm^2 in $BiFeO_3$ Thin Film*Jpn. J. Appl. Phys*. Vol. 43, 2004 pp. L647-L648.

[11] Bibes, M.; and Barthelemy, A.; (2008) Towards a magnetoelectric memory*Nature materials*, Vol. 7, 2008 pp. 425-426.

[12] Ramesh, R.; and Spaldin, N. A. (2007) Multiferroics: progress and prospects in thin films *Nature materials*, Vol. 6, 2007 pp. 21-29.

[13] Chu, Y. H.; Martin, L. W.; Holcomb, M. B.; Gajek, M.; Han, S. –J.; He, Q.; Balke, N.; Yang, C. –H.; Lee, D.; Hu, W.; Zhan, Q.; Yang, P. –L.; Rodriguez, A. F.; Scholl, A.; Wang, S. X.; and Ramesh, R.; (2008) Electric-field control of local ferromagnetism using a magnetoelectric multiferroic*Nature materials*, Vol. 7, 2008, pp. 478-482.

[14] Iakovlev, S.; Solterbeck, C. –H.; Kuhnke, M.; and Es-Souni, M.; (2005) Multiferroic $BiFeO_3$ thin films processed via chemical solution deposition: Structural and electrical characterization *J. Appl. Phys.*, Vol. 97, 2005 pp. 094901-1-094901-6.

[15] Kumar, A.; Rai, R. C.; Podraza, N. J.; Denev, S.; Ramiez, M.; Chu, Y. –H.; Martin, L. W.; Ihlefeld, J.; Heeg, T.; Schubert, J.; Schlom, D. G.; Orenstein, J.; Ramesh, R.; Collins, R. W.; Musfeldt, J. L.; and Gopalan, V.; (2008) Linear and nonlinear optical properties of $BiFeO_3$ *Appl. Phys. Lett.*, Vol. 92, 2008, pp. 121915-1-121915-3.

[16] Choi, T.; Lee, S.; Choi, Y. J.; Kiryukhin, V.; and Cheong, S. –W. (2009) Switchable Ferroelectric Diode and Photovoltaic Effect in $BiFeO_3$ *Science* Vol. 324, 2009, pp. 63-66.

[17] Kiselev, S. V.; Ozerov, R. P.; and Zhdanov, G. S.; (1963) Sov. Phys., Vol. 7 1963, pp. 742.

[18] Venevtsev, Yu. N.; Zhadanow, G.; and Solov'ev, S.; (1960) Sov. Phys. Crystallogr., Vol. 4 1960, pp. 538.

[19] Kubel, F.; and Schmid, H.; (1990) Structure of a Ferroelectric and Ferroelastic Monodomain Crystal of the Perovskite $BiFeO_3$ *Acta Crystallogr. B*, Vol. 46 1990, pp. 698-702.

[20] Filip'ev, V. S.; Smol'yaninov, I. P.; Fesenko. E. G.; and Belyaev, I. I.; Kristallografiya, Vol. 5 1960 pp. 958.

[21] Dzyaloshinskii, I. E.; S(1957) Sov. Phys. JETP, Vol. 5 1957 pp. 1259.

[22] Moriya, T. (1960) Anisotropic superexchange interaction and weak ferromagnetism *Phys. Rev.*, Vol. 120, 1960 pp. 91-98.

[23] Neaton, J. B.; Ederer, C.; Waghmare, U. V.; Spaldin, N. A.; and Rabe, K. M.; (2005) First-principles study of spontaneous polarization in multiferroic $BiFeO_3$ *Rhys. Rev. B*, Vol. 71 2005 pp. 014113-1-014113-8.

[24] Ederer, C.; and Spaldin N. A. (2005) Effect of Epitaxial Strain on the Spontaneous Polarization of Thin Film Ferroelectrics, *Physical Review Letters.*, Vol. 95, December 2005, pp. 257601-1-4.

[25] Teague, J. R.; Gerson, R.; and James, W. J.; (1970) Dielectric Hysteresis in single crystal $BiFeO_3$ *Solid State Commun.*, Vol. 8 1970 pp. 1073-1074.

[26] Schwartz, R. W. (1997) Chemical Solution Deposition of Perovskite Thin Films *Chem. Mater.*, Vol. 9 1997 pp. 2325-2340.

[27] Aspnes, D. E. (1974) Optimizing precision of rotating-analyzer ellipsometers *J. Opt. Soc. Am.*, Vol. 64 1974 pp. 639-646.

[28] Jayatissa, A. H.; Suzuki, M.; Nakanishi, Y.; and Hatanaka, Y. (1995) Microcrystalline structure of poly-Si films prepared by cathode-type r.f. glow discharge *Thin Solid Films*, Vol. 256 1995 pp. 234-239.

[29] Yao, H.; Snyder, P. G.; and Woollam, J. A.; (1991) Temperature dependence of optical properties of GaAs *J. Appl. Phys*., Vol. 70 1991 pp. 3261-3267.

[30] Yao, H.; Woollam, J. A.; and Alterovitz, S. A.; (1993) Spectroscopic ellipsometry studies of I-IF treated Si (100) surfaces *Appl. Phys. Lett*., Vol. 62 1993 pp.3324-3326.

[31] Brendel, R.; and Bormann, D.; (1992) An infrared dielectric function model for amorphous solids *J. Appl. Phys*., Vol. 71 1992 pp. 1-6.

[32] Kim, C. C.; Garland, J. W.; Abad, H.; and Raccah, P. M.; (1992) Modeling the optical dielectric function of semiconductors: extension of the critical0point parabolic-band approximation *Phys. Rev. B*, Vol. 45 1992 pp. 11749-11767.

[33] Khan, M. H.; Shen, H.; Xuan, Y.; Zhao, L.; Xiao, S.; Leaird, D. E.; Weiner, A. M.; and Qi, M. (2010) Ultrabroad-bandwidth arbitrary radiofrequency waveform generation with a silicon photonic chip-based spectral shaper *Nature Photonics*, Vol. 4 2010 pp. 117-122.

[34] Yamada, H.; Chu, T.; Ishida, S.; and Arakawa, Y. (2006) Si Photonic Wire Waveguide Devices *IEEE Journal of selected topics in quantum electronics*, Vol. 12 2006 pp. 1371-1378.

[35] Wang, X.; Xu, L.; Li, D.; Liu, L.; and Wang, W.; (2003) Thermo-optic properties of sol-gel-fabricated organic–inorganic hybrid waveguides *J. Appl. Phys*., Vol. 94 2003 pp. 4228-4230.

[36] Naganuma. H.; Inoue, Y.; and Okamura, S.; (2008) Evaluation of Electrical Properties of Leaky $BiFeO_3$ Films in High Electric Field Region by High-Speed Positive-Up–Negative-Down Measurement *Appl. Phys. Exp*., Vol. 1 2008 pp. 061601-1-061601-3.

[37] Landauer, R.; in Electrical Transport and Optical Properties of Inhomogeneous Media, ed. J. C. Garland and D. B. Tanner (AIP, New York, 1979) p. 1.

[38] Ting, C. –C.; Chen, S. –Y.; and Liu, D. –M.; (2000) Structural evolution and optical properties of TiO_2 thin films prepared by thermal oxidation of sputtered Ti films *J. Appl. Phys*., Vol. 88 2000 pp. 4628-4633.

[39] Ihlefeld, J. F.; Podraza, N. J.; Liu, Z. K.; Rai, R. C.; Xu, X.; Heeg, T.; Chen, Y. B.; Li, L.; Collins, R. W.; Musfeldt, J. L.; Pan, X. Q.; Schubert, J.; Ramesh, R.; and Schlom, D. G. (2008) Optical band gap of $BiFeO_3$ grown by molecular-beam epitaxy *Appl. Phys. Lett*., Vol. 92 2008 pp. 908-1-908-3.

[40] Hauser, A. J.; Zhang, J.; Mier, L.; Ricciardo, R. A.; Woodward, P. M.; Brillson, L. J.; and Yang, F. Y.; (2008) Characterization of electronic structure and defect states of thin epitaxial $BiFeO_3$ films by UV-visible absorption and cathodoluminescence spectroscopies *Appl. Phys. Lett*., Vol. 92 2008 pp. 222901-1-222901-3.

[41] Pankove, J. I.; Optical Process in Semiconductors (Prentice-Hall, Englewood Cliffs, NJ, 1971) p. 34.

[42] Amirov, A. A.; Batdalov, A. B.; Kallaev, S. N.; Omarov, Z. M.; Verbenko, I. A.; Razumovskaya, O. N.; Reznichenko, L. A.; and Shilkina, L. A.; (2009) Specific Features of the Thermal, Magnetic, and Dielectric Properties of Multiferroics $BiFeO_3$ and $Bi_{0.95}La_{0.05}FeO_3$ *Phys. Solid State*, Vol. 51 2009 pp. 1189-1192.

[43] Watanabe, H.; Yamada, N.; and Okaji, M. (2004) Linear Thermal Expansion Coefficient of Silicon from 293 to 1000 K *Inter. J. Thermophys*., Vol. 25 2004 pp. 221-236.

[44] Okada, Y.; and Tokumaru, Y.; (1984) Precise determination of lattice parameter and thermal expansion coefficient of silicon between 300 and 1500 K *J. Appl. Phys*., Vol. 56 1984 pp. 314-320.

[45] Zhang, Z.; Zhao, P.; Lin, P.; and Sun, F.; (2006) Thermo-optic coefficients of polymers for optical waveguide applications *Polymer*, Vol. 47 2006 pp. 4893-4896.

[46] Jewell, J. M.; Askins, C.; and Aggarwal, D. (1991) Interferometric method for concurrent measurement of thermo-optic and thermal expansion coefficients *Appl. Opt*., Vol. 30 1991 pp. 3656-3660.

IntechOpen